



OPEN ACCESS

EDITED BY

Ahmed A. Zaki Diab,
Minia University, Egypt

REVIEWED BY

Daniel Fodorean,
Technical University of Cluj-Napoca, Romania
Norjulia Mohamad Nordin,
University of Technology Malaysia, Malaysia

*CORRESPONDENCE

Ayokunle Awelewa,
✉ ayokunle.awelewa@
covenantuniversity.edu.ng

RECEIVED 06 June 2024

ACCEPTED 12 September 2024

PUBLISHED 03 October 2024

CITATION

Balogun A, Olajube A, Awelewa A, Okafor F,
Sanni T and Samuel I (2024) A
sensorless efficiency-optimizing vector control
scheme for an induction motor drive.
Front. Energy Res. 12:1406565.
doi: 10.3389/fenrg.2024.1406565

COPYRIGHT

© 2024 Balogun, Olajube, Awelewa, Okafor,
Sanni and Samuel. This is an open-access article
distributed under the terms of the [Creative
Commons Attribution License \(CC BY\)](#). The use,
distribution or reproduction in other forums is
permitted, provided the original author(s) and
the copyright owner(s) are credited and that the
original publication in this journal is cited, in
accordance with accepted academic practice.
No use, distribution or reproduction is
permitted which does not comply with these
terms.

A sensorless efficiency- optimizing vector control scheme for an induction motor drive

Adeola Balogun¹, Ayobami Olajube², Ayokunle Awelewa^{3*},
Frank Okafor¹, Timilehin Sanni³ and Isaac Samuel³

¹Department of Electrical and Electronics Engineering, University of Lagos, Lagos, Nigeria, ²Department of Electrical and Computer Engineering, Florida State University, Tallahassee, FL, United States, ³Department of Electrical and Information Engineering, Covenant University, Ota, Ogun, Nigeria

In this paper, an energy-saving scheme in rotor field-orientated vector control is developed for induction motor drives. The energy-saving scheme minimizes copper and core losses in induction motors, which are equally applicable to induction generators. In efficiency optimization, an optimal stator angular velocity is uniquely obtained, and consequently, a corresponding optimal slip at any given rotor speed is determined. The challenge of determining a reference for rotor flux linkage that guarantees the minimal copper and core loss regime is overcome by developing a load torque observer loop. The torque observer is developed alongside a rotor speed observer for a sensorless speed operation. The observed mechanical torque is further used to enhance the outer-loop rotor speed control that generates an electromagnetic torque command used in building the reference for the inner-loop stator current control. The results obtained justified the effective operation of the torque and rotor speed observer, which consequently verified the effective minimal electrical loss regime at the optimal stator angular velocity and optimal rotor flux linkage. The results are further compared to results obtained from the equivalent induction machine drive on a finite-set model predictive control (FS-MPC) scheme with the same values of the optimal stator angular velocity and optimal rotor flux linkage. The developed efficiency-optimized vector control scheme gave lower ripples in developed electromagnetic torque and dampened overshoot better during step change in load torque.

KEYWORDS

vector control, stator speed, rotor flux, optimum speed, optimization, three-phase voltage source inverter, power loss

1 Introduction

Over the years, induction machines, particularly squirrel cage induction motors, have maintained dominance in various industrial manufacturing and domestic applications. The squirrel cage induction motors have been competitive machines of choice for industrial electric drives because they are very rugged, relatively cheaper, and have low maintenance requirements than the wound rotor type. However, induction machines in general should be operated in least loss regimes to avoid over-consumption of energy. Kirischen et al. (1987) stated that electric drives have the largest share of grid energy consumption in the world. Hence, improved efficiencies in energy utilization by induction motors yield tremendous savings, and consequently, they avail more energy to other consumers. As such, efficiency improvement in induction motors significantly contributes to reduction in

production costs in the manufacturing sector. Other applications that benefit tremendously from efficiency optimization in induction motors include motor-driven compressors in heating, ventilation, and air conditioning (HVAC) systems and in electric vehicle applications (Ghozziandall et al., 2004; Sajedi et al., 2011).

Core (iron) and copper (resistive) losses are the main electrical losses, which must be tactically minimized for energy savings to occur significantly in an induction machine drive (Abrahamsen et al., 2001). Minimization of such electrical losses is more than often implemented via adjustable voltage and frequency/speed control methods. With the advent of power electronics inverters, adjustable speed drives have been more competitive in industrial automation than their fixed-speed counterparts, where reasonable efficiency can only be achieved at full load (Kirschen et al., 1984; Sul and Park, 1988; Kirschen et al., 1985; Vukosavic and Levi, 2003).

Several control techniques have been employed to improve the efficiency of induction motor drives (Abrahamsen et al., 1996). They are grouped into three major categories: simple state control (SSC) (Akin et al., 2004; Lascu and Trzynadlowski, 2004), loss model control (LMC) (Uddin and Nam, 2008; Olajube and Anubi, 2023; Uddin et al., 2019), and the search control (SC) algorithms (Rehman and Xu, 2011; Kastha and Bose, 1995; Choudhary et al., 2015). The LMC involves the use of a machine model to compute the losses by selecting an appropriate value of flux that minimizes these losses, and it is the fastest of the three methods. However, its major drawback is its sensitivity to parameter variations. The SSC, on the other hand, is the simplified version of the LMC that utilizes the state-space control technique, which may include observer design to estimate the value of the required flux for cost and loss minimization (Almeida et al., 2007). SC is devoid of parameter variations but suffers from torque ripples and slow convergence depending on the dimension of its dynamics (Vukosavic and Levi, 2003; Chakraborty and Hori, 2003; Blanusa, 2010). Prior knowledge of the machine parameters is also required by the SC method for proper variation of the flux to achieve an optimum operating condition. However, these methods can be hybridized or combined to forestall the shortcomings of the individual methods (Chakraborty and Hori, 2003; Blanusa, 2010; Qu et al., 2012; Stumper et al., 2013). A fuzzy logic control method was used in Kumar et al. (2014) for fast convergence of the search control technique and to prevent torque ripples. A neuro-fuzzy method was also used in Sousa et al. (1995) and Bose et al. (1997) to improve the fuzzy logic technique.

The convergence point for the least core loss in an induction machine will not necessarily correspond to the convergence point for the least copper loss, as the two losses attain their minimal values independently. Therefore, to achieve an operating regime where both losses can be considered adequately reduced, a compromise between the core and copper losses must be reached. A compromise will be reached where both losses intersect.

In this article, therefore, classical Jacobi is used as the loss minimization procedure to uniquely determine the point of intersection between the core and copper losses. Consequently, the loss minimization yielded an optimal rotor flux command and an optimal stator angular velocity that fixes operation to a constant slip operation. Hence, the loss minimization in this paper is implemented via the field-orientated vector control scheme. In general, vector control is a multivariable control scheme that can

target more than one control objective, which has matured significantly over the years. It has capability for flux regulation used in efficiency improvement, which makes it very promising in industrial drives (Chakraborty and Hori, 2003; Ta-Cao and Hori, 2000; Chakraborty et al., 2003; Moreno-Eguilaz and Peracaula, 1999; Sousa et al., 1992). However, a major setback with vector control is sensitivity to system parameter mismatch (Balogun et al., 2021). Mismatched inductance in the cross-coupling terms of the inner loop current control was observed in Balogun et al. (2021) to majorly influence the stability of the system. The setback in such system parameter mismatch is mitigated in this article by increasing the gains of the proportional plus integral (PI) of the inner loop control, as shown in Balogun et al. (2021). Such a strategy is adopted herein to improve the resiliency of vector control to system parameter variation. Furthermore, observers will be introduced to eliminate the need for mechanical sensors for rotor speed and mechanical load torque. The observed mechanical torque variable will be fed forward to enhance the rotor speed control loop in obtaining the reference command for inner current loop control. Furthermore, a comparative analysis is done between the developed vector control and equivalent finite-set model predictive control (FS-MPC) on an equivalent induction machine.

The rest of the paper is arranged as follows: Sections 2 and 3 present the model of an induction machine and its steady-state analysis, respectively. Electrical loss minimization control laws are discussed in Section 4, while the design of the efficiency-optimizing dynamic control scheme is shown in Section 5. Section 6 focuses on the mechanical torque and rotor speed observer design. The results and comparative analyses are given in Section 7 along with the discussion, and the paper is concluded in Section 8.

2 Induction machine model

An inverter-fed squirrel cage induction motor is illustrated in Figure 1A. The dynamic model of the squirrel cage induction motor drive is given in Equation 1–11. In Equation 1, Equation 2, $k_c = 1 + (r_s/r_c)$, whereby the stator voltage equations account for the core loss with a core loss resistance r_c , as shown in Figure 1B. Therefore, i'_{qs} and i'_{ds} are the effective torque producing stator current, as defined in Balogun et al. (2021) and Gong et al. (2019). Therefore, they are referred to as the stator currents to avoid confusion in use of terms.

$$v_{qs} = \frac{m_{qs}v_{dc}}{2} = r_s i'_{qs} + k_c p \lambda_{qs} + k_c \omega \lambda_{ds} \tag{1}$$

$$v_{ds} = \frac{m_{ds}v_{dc}}{2} = r_s i'_{ds} + k_c p \lambda_{ds} - k_c \omega \lambda_{qs} \tag{2}$$

$$v_{qr} = 0 = r_r i_{qr} + p \lambda_{qr} + (\omega - \omega_r) \lambda_{dr} \tag{3}$$

$$v_{dr} = 0 = r_r i_{dr} + p \lambda_{dr} - (\omega - \omega_r) \lambda_{qr} \tag{4}$$

where

$$\lambda_{qs} = L_s i'_{qs} + L_m i_{qr} \tag{5}$$

$$\lambda_{ds} = L_s i'_{ds} + L_m i_{dr} \tag{6}$$

$$\lambda_{qr} = L_r i_{qr} + L_m i'_{qs} \tag{7}$$

$$\lambda_{dr} = L_r i_{dr} + L_m i'_{ds} \tag{8}$$

$$p\omega_r = \frac{P}{2J} (T_e - T_m) \tag{9}$$

where

$$T_e = \frac{3PL_m}{4L_r} (\lambda_{dr} i'_{qs} - \lambda_{qr} i'_{ds}). \quad (10)$$

$$C_d p v_{dc} = \frac{3}{2} (i_o - i_d) = \frac{3}{2} i_o - \frac{3}{4} (m_{qs} i_{qs} + m_{ds} i_{ds}). \quad (11)$$

3 Steady-state analysis

In general, steady-state analysis is quite useful in establishing the operating and boundary regions in electric machines. Particularly, in squirrel cage induction motor drive, a regulation of the operational stator angular velocity (ω , in arbitrary reference frame) is of significant interest for achieving energy savings. At steady state, the derivative elements in the model of Section 2 are set to 0. Therefore, use of the steady states of Equations 3, 4 for appropriate substitution in rotor flux linkages in the T_e of the steady-state of Equation 9 yields Equation 12, which can be re-evaluated as Equation 13.

$$T_e = T_m = \frac{3P}{4} \left(\frac{r_r I_r^2}{(\omega - \omega_r)} \right). \quad (12)$$

$$I_r^2 = \frac{4(\omega - \omega_r)}{3Pr_r} T_e = \frac{4(\omega - \omega_r)}{3Pr_r} T_m. \quad (13)$$

$$P_L = \frac{3}{2} [(I_{qs}^2 + I_{ds}^2)r_s + (I_{qr}^2 + I_{dr}^2)r_r + (I_{cq}^2 + I_{cd}^2)r_c]. \quad (14)$$

$$P_L = \left(a_{PL} + \frac{b_{PL}\omega}{(\omega - \omega_r)} + \frac{c_{PL}}{(\omega - \omega_r)^2} \right) I_r^2. \quad (15)$$

Here,

$$a_{PL} = \frac{3}{2} \left[\frac{L_s}{L_m^2} (L_s^2 (r_r - r_c) - r_r) - 2L_s L_r (r_r + r_c) + r_r + r_s L_m + L_m^2 r_c \right],$$

$$b_{PL} = \frac{3r_r r_c}{2L_m}, \text{ and } c_{PL} = \frac{3}{2L_m^2} [r_s r_r^2 (1 + L_s^2) + r_c L_s^2].$$

The core and copper losses (P_L) of the machine are combined and given in Equation 14. The first two terms in Equation 14 give the copper loss, while the last term gives the core loss. The two loss regimes are embedded into Equation 14 so that two separate objective functions can be evaluated at once. If an induction machine is made to operate at constant slip when there is no magnetic saturation, as the rotor current increases, the stator angular velocity increases, and the copper loss increases while the core loss decreases. The two losses run contrary, as shown in Figure 2A. As such, a region of compromise must be reached where both loss functions intersect, which will be agreeable as optimal, as seen in Figure 2A. Consequently, at the point of intersection, the contribution of each of the loss function takes 50%, which implies that each of the copper loss and the core loss contributes equally to the total electrical losses at the optimal point. Therefore, Equation 14 is evaluated further as Equation 15, by appropriate substitution and simplification, to have reduced variable sets like Equation 12. By implication, substituting Equation 13 into Equation 15 gives the P_L as a quadratic function of ω , which gives rise to an optimization

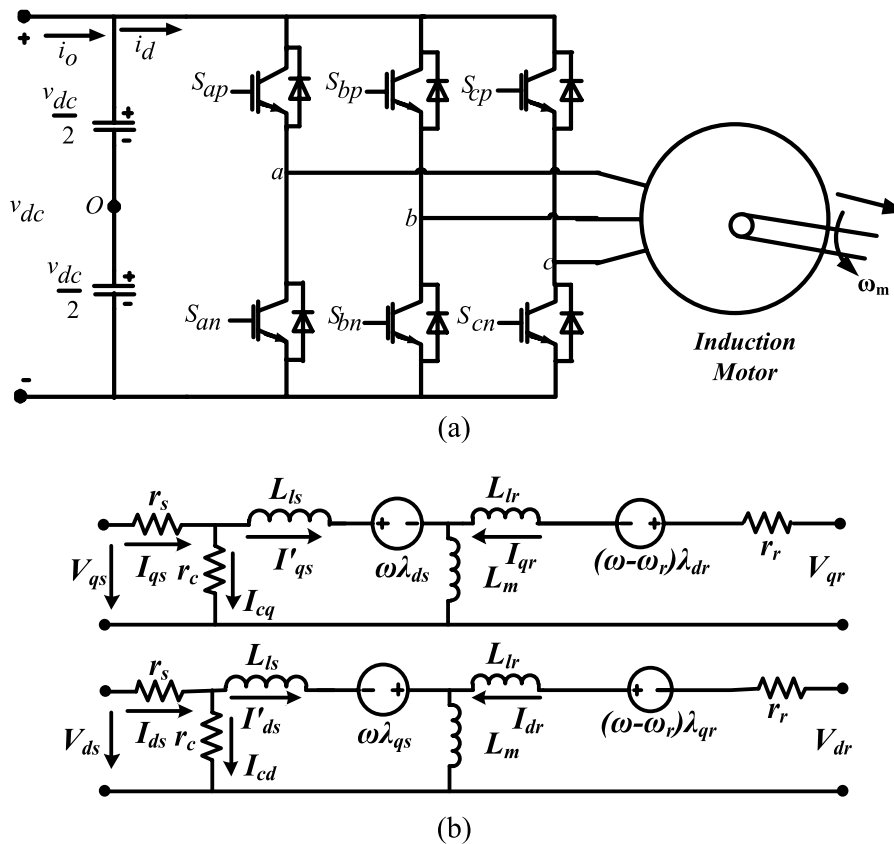


FIGURE 1 (A) An inverter-fed induction motor drive system. (B) $q-d$ equivalent circuit model of the induction machine including core-loss resistance.

problem of minimizing the operational electrical losses at a corresponding stator angular velocity. As such, an optimization procedure that uniquely determines ω is given in the next section.

In Figures 2B, C, profiles of the variation of P_L against stator angular velocity (ω) and against slip angular velocity (ω_s) are given, respectively, at specified electromagnetic (T_e) or mechanical (T_m) torque and rotor speed (ω_r). The plots were obtained while the machine is constrained not to exceed the rated stator voltage and current (i.e., $V_s = \sqrt{V_{qs}^2 + V_{ds}^2} \leq V_{s_rated}$ and $I_s = \sqrt{I_{qs}^2 + I_{ds}^2} \leq I_{s_rated}$).

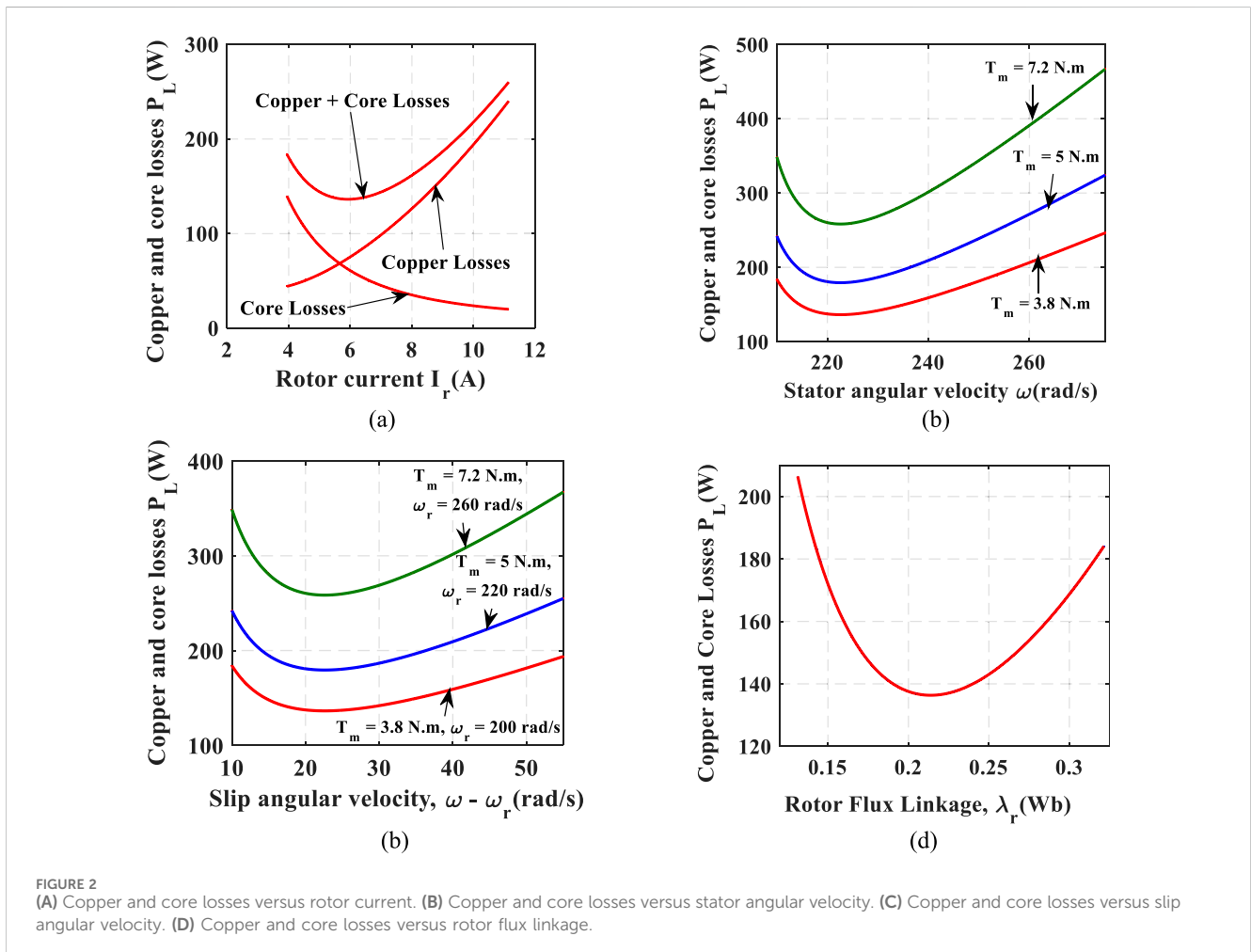
In Figure 2B, the rotor speed was specified at 200 rad/s for the random T_m at 3.8 N.m, 5 N.m, and 7.2 N.m. It can be seen in the figure that the least P_L at each of the given T_m coincides at the same ω of 224 rad/s. Therefore, there exists a constant slip angular velocity given as $s\omega$ (where $s\omega = \omega - \omega_r$, obtained from slip $s = ((\omega - \omega_r)/\omega)$, which is 24 rad/s. As such, the constant slip operation for least P_L is further justified in Figure 2C, where the three given T_m in Figure 2B are subjected to random sub-synchronous ω_r . Consequently, the least P_L in each of the plot still coincides to 24 rad/s. In Figure 2D, the rotor flux linkage, regardless of the rotor speed, has a unique minimal value of 0.208 Wb that corresponds to less power loss. This value is observed to change only when the T_m (and consequently T_e) changes.

4 Electrical loss minimization control laws

In the previous section, the optimization problem was established as a control problem with an objective function of minimizing the copper and core losses of the induction machine with respect to the stator angular velocity and the rotor current magnitude. The goal is to investigate if a unique expression can be determined for an optimal stator angular velocity and consequently obtaining a unique expression for an optimal rotor flux linkage reference.

4.1 Determination of optimal stator frequency

The classical Jacobi is employed for the optimization procedure, which is formulated from the derivatives of P_L and T_e with respect to ω and I_r , as given in Equation 16. The objective (cost) function of Equation 16 is to minimize P_L , which also corresponds to maximizing the torque or power output of the machine. With the determinant of Equation 16 set to 0, Equation 17 is obtained as an optimal stator angular velocity that fixes the slip at an optimal value. The optimal stator angular velocity is critical for constant slip operation. As such, with machine parameters given in the appendix,



Equation 17 gives $\omega_{opt} = 224 \text{ rad/s}$ with rotor speed set at 200 rad/s , which corresponds to the value obtained as optimal in Figure 2B. Consequently, the terms in square root in the right-hand side of Equation 17 correspond to the slip angular velocity ω_s , which is fixed at 24 rad/s according to the parameters of the test machine of this paper.

$$\begin{vmatrix} \frac{dT_e}{dI_r} & \frac{dT_e}{d\omega} \\ \frac{dP_L}{dI_r} & \frac{dP_L}{d\omega} \end{vmatrix} = 0. \quad (16)$$

$$\omega_{opt} = \omega_r \pm \sqrt{\frac{A_c}{B_c}}. \quad (17)$$

Here, $A_c = r_c r_r^2 (1 + L_s^2) + r_c^2 r_r^2 L_s^2$ and $B_c = r_c r_s (1 + L_s^2) L_r^2 - 2r_c r_s L_s L_r L_m^2 + 2r_s r_r L_m^2 + r_c r_r L_m^2 + r_c^2 L_s^2 L_r^2 - 2r_c^2 L_s L_r L_m^2 + r_c^2 L_m^4$

4.2 Determination of optimal rotor flux linkage

With an optimal stator angular velocity obtained, a corresponding optimal rotor flux linkage reference can consequently be determined. Notice that at steady state of Equation 4 and with a rotor flux alignment of $\lambda_{qr} = 0$ and $\lambda_{dr} = \lambda_r$, $I_{dr} = 0$, consequently, $I_{qr} = I_r$. Therefore, the steady state of Equation 3, 18 is obtained, while Equation 19 is determined from Equation 13. As such, the corresponding optimal rotor flux linkage is given in Equation 20 as 0.208 Wb , with the mechanical torque specified as 3.8 N.m and with an optimal slip angular velocity obtained as 24 rad/s for this machine in the last sub-section. Therefore, based on Equation 20, the rotor flux agrees with Figure 2D and will only change along an optimal profile determined by a change in the mechanical torque.

$$\lambda_{dr} = -\frac{r_r I_{qr}}{\omega_{opt} - \omega_r}. \quad (18)$$

$$I_{qr} = \sqrt{\frac{4T_m(\omega_{opt} - \omega_r)}{3Pr_r}}. \quad (19)$$

$$\lambda_{dr-opt} = \pm \sqrt{\frac{4T_m r_r}{3P(\omega_{opt} - \omega_r)}} = 0.208 \text{ Wb}. \quad (20)$$

5 Efficiency-optimizing dynamic control scheme

The energy-saving dynamic control scheme is based on rotor flux-oriented vector control with inner-loop stator current control and outer-loop speed and rotor flux control. The rotor flux orientation of $\lambda_{qr} = 0$ and $\lambda_{dr} = \lambda_r$ used in the previous section is adopted in the dynamic control. The flux alignment decouples inner-loop control of electromagnetic torque via independent control on the q-axis.

5.1 Inner-loop current control

The stator equations in Equations 1, 2 form the basis for the inner-loop control with the voltage impressed by the inverter as the stator control input vectors. As such, the stator flux linkages in Equations 1, 2 are expressed in terms of the rotor flux linkages and the stator current for the rotor field-oriented control. Consequently, Equation 21 is obtained as the dynamics of the inner-loop current regulation and expressed in complex form, as given in Equation 22.

$$\begin{bmatrix} L_\sigma p i_{qs} + r i_{qs} \\ L_\sigma p i_{ds} + r i_{ds} \end{bmatrix} = \begin{bmatrix} \delta_{qs} \\ \delta_{ds} \end{bmatrix} = \begin{bmatrix} -\frac{\omega_r L_m \lambda_{dr}}{L_r} - \omega L_\sigma i_{ds} \\ \frac{r_r L_m \lambda_{dr}}{L_r^2} + \omega L_\sigma i_{qs} \end{bmatrix} + \begin{bmatrix} \frac{1}{k_c} & 0 \\ 0 & \frac{1}{k_c} \end{bmatrix} \begin{bmatrix} v_{qs} \\ v_{ds} \end{bmatrix}. \quad (21)$$

$$(L_\sigma p + r) i_{qds} = K_r (i_{qds}^* - i_{qds}) = K_r (e_{qds}) = \delta_{qds}. \quad (22)$$

Here, $r = (r_s/k_c) + (r_r L_m^2/L_r^2)$ and $L_\sigma = L_s - L_m^2/L_r$.

$$G_r(p) = \frac{i_{qs}}{K_{qr} e_{qs}} = \frac{i_{ds}}{K_{dr} e_{ds}} = \frac{1}{(pL_\sigma + r)}. \quad (23)$$

Expanding Equation 22 gives the open-loop current transfer function of Equation 23, where $K_{qr} = K_{dr} = K_r$ and represents the proportional plus integral (PI) controllers in the inner-loop. The delay given in Equation 24 accounts for dead-time and transport/sampling delays introduced by the inverter feeding the machine and the analog-to-digital conversion process (Balogun et al., 2021; Dong and Ojo, 2006; Holmes et al., 2009; Kazmierkowski et al., 2002; Rabelo et al., 2009). Introducing Equations 24, 23 yields Equation 25. With the PI controller K_r expressed in terms of proportional and integral gains in Equation 26, the closed-loop transfer function of the plant's inner-loop current control is given by Equation 27. For pole zero cancellation, the controller's gains are selected such that $K_{pr}/K_{ir} = L_\sigma/r$ (Lascu et al., 2007). Since inner-loop current controllers are the most significant in vector control stability (Ali et al., 2020), the stability of Equation 27 is sacrosanct.

$$G_d(p) = \frac{1}{(pT_{rd} + 1)}. \quad (24)$$

$$G_r(p)G_d(p) = \frac{1}{(pL_\sigma + r)} \cdot \frac{1}{(pT_{rd} + 1)}. \quad (25)$$

$$K_r(p) = \frac{pK_{pr} + K_{ir}}{p}. \quad (26)$$

$$G_{cr}(p) = \frac{K_{pr}}{(p^2 L_\sigma T_{rd} + pL_\sigma + K_{pr})}. \quad (27)$$

Comparing the denominator of Equation 27 with the second-order Butterworth polynomial of $p^2 + 2\omega_n \zeta p + \omega_n^2$ at optimal damping criteria, such that $\zeta = 1/\sqrt{2}$, then $\omega_n/\sqrt{2} = 1/T_{rd}$ and $\omega_n^2 = K_{pr}/(L_\sigma T_{rd})$. Therefore, $K_{pr} = L_\sigma/(2T_{rd})$, and consequently, $K_{ir} = r/(2T_{rd})$. Hence, Equation 27 is further simplified as Equation 28. As such, the control inputs from the inverter are the stator voltage vectors given in Equation 29. δ_{qs} and δ_{ds} in Equation 29 stand for outputs from K_{qr} and K_{dr} in the q-axis and d-axis, respectively.

$$G_{cr}(p) = \frac{i_{qs}}{i_{qs}^*} = \frac{i_{ds}}{i_{ds}^*} = \frac{1}{(p^2 2T_{rd}^2 + p2T_{rd} + 1)}. \quad (28)$$

$$\begin{bmatrix} v_{qs} \\ v_{ds} \end{bmatrix} = \begin{bmatrix} \frac{1}{k_c} & 0 \\ 0 & \frac{1}{k_c} \end{bmatrix}^{-1} \left[\begin{bmatrix} \delta_{qs} \\ \delta_{ds} \end{bmatrix} - \begin{bmatrix} \frac{\omega_r L_m \lambda_{dr} - \omega L_{\sigma} i_{ds}}{L_r} \\ \frac{r_r L_m \lambda_{dr} + \omega L_{\sigma} i_{qs}}{L_r} \end{bmatrix} \right]. \quad (29)$$

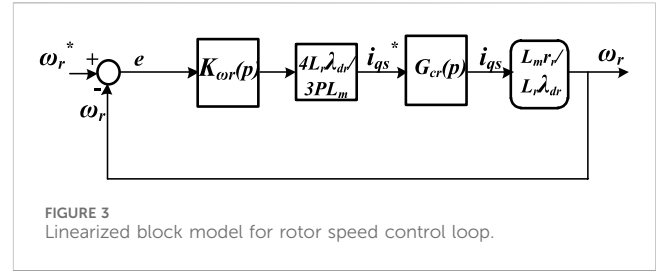


FIGURE 3 Linearized block model for rotor speed control loop.

5.2 Outer-loop speed control

The rotor speed outer-loop control is developed from Equation 9 and obtained in Equation 30. With the rotor field orientation in the electromagnetic torque, as given in Equation 31, and accounting for friction and windage losses in Equation 9 via damping coefficient B_m , Equation 30 is expanded to Equation 32. Consequently, the q-axis stator current reference is generated in Equation 33. The current reference can also be represented by Equation 34 from Equation 28. As such, Equation 32 is modified to Equation 35. Equation 36 is obtained from Equation 3 and substituted in Equation 35 to yield Equation 37, which results in the open-loop transfer function of Equation 38. In the closed loop, Equation 39 evolves from Equation 38. $K_{\omega r}$ is the PI controller for the outer rotor speed loop, and $\delta_{\omega r}$ stands for the output of $K_{\omega r}$.

$$\frac{2J}{P} p\omega_r = (T_e^* - T_m) = K_{\omega r} (\omega_r^* - \omega_r) = K_{\omega r} (e_{\omega}) = \delta_{\omega}. \quad (30)$$

$$T_e = \frac{3PL_m}{4L_r} \lambda_{dr} i_{qs}^*. \quad (31)$$

$$\begin{aligned} \frac{2J}{P} p\omega_r + \frac{2}{P} B_m \omega_r &= \left(\frac{3PL_m}{4L_r} \lambda_{dr} i_{qs}^* - T_m \right) = K_{\omega r} (\omega_r^* - \omega_r) = K_{\omega r} (e_{\omega r}) \\ &= \delta_{\omega r}. \end{aligned} \quad (32)$$

$$i_{qs}^* = \frac{L_r}{k\lambda_r L_m} (\delta_{\omega r} + T_m). \quad (33)$$

$$i_{qs}^* = i_{qs} (p^2 2T_{rd}^2 + p2T_{rd} + 1). \quad (34)$$

$$K_{\omega r} (\omega_r^* - \omega_r) = \frac{3PL_m}{4L_r} \lambda_{dr} i_{qs} (p^2 2T_{rd}^2 + p2T_{rd} + 1) - T_m. \quad (35)$$

$$i_{qs} = \frac{L_r}{L_m r_r} \lambda_r (\omega - \omega_r). \quad (36)$$

$$K_{\omega r} (\omega_r^* - \omega_r) = \frac{3P}{4r_r} \lambda_r^2 (\omega - \omega_r) (p^2 2T_{rd}^2 + p2T_{rd} + 1) - T_m. \quad (37)$$

$$H_{o\omega r} = \frac{\omega_r}{K_{\omega r} (\omega_r^* - \omega_r)} = \frac{\omega_r}{K_{\omega r} e_{\omega r}} = k_o \frac{1}{(p^2 2T_{rd}^2 + p2T_{rd} + 1)}. \quad (38)$$

Here, $k_o = \frac{-3P}{4r_r} \lambda_r^2$.

$$H_{c\omega r} = k_o \frac{K_{\omega r}}{(p^2 2T_{rd}^2 + p2T_{rd} + 1)(pT_{rc} + 1) + k_o K_{\omega r}}. \quad (39)$$

In order make the controller's zero cancel the undesired pole of the plant (Lascu et al., 2007), let the gains of the PI controller design in Equation 40 be selected as Equation 41 to yield Equation 42.

$$K_{\omega r} = K_{p\omega r} + \frac{K_{i\omega r}}{p}. \quad (40)$$

$$\frac{K_{p\omega r}}{K_{i\omega r}} = \frac{J}{B_m}. \quad (41)$$

$$K_{\omega r} = \frac{K_{p\omega r}}{pT_{i\omega r}} (T_{i\omega r} p + 1). \quad (42)$$

Here, $T_{i\omega r} = J/B_m$.

Hence, appropriate substitution of Equation 42 in Equation 39, while equating that $T_{i\omega r} = T_{rc}$, $K_{p\omega r} = \frac{T_{rc}}{2k_o T_{rd}}$, and $k_o = \frac{-3P}{4r_r} \lambda_r^2$, yields the overall closed-loop transfer function of the speed control in Equation 43, given that all other disturbances are equated to 0. The linearized block model of the speed control loop is given in Figure 3.

$$H_{c\omega r} = \frac{1}{p^3 4T_{rd}^3 + p^2 4T_{rd}^2 + p2T_{rd} + 1}. \quad (43)$$

5.3 Outer-loop optimized rotor flux linkage control

The rotor flux linkage is regulated at the outer-loop d -axis control of the inverter. Equation 44 evolves from Equation 4 and yields Equation 45 as the dynamics for the flux regulation. Therefore, Equation 28 yields Equation 46.

$$L_r p\lambda_{dr} + r_r \lambda_{dr} = r_r L_m i_{ds}^* \quad (44)$$

$$\delta_{\lambda r} = K_{\lambda r} (\lambda_{dr}^* - \lambda_{dr}) = K_{\lambda r} (e_{\lambda r}) = (L_r p + r_r) \lambda_{dr} = r_r L_m i_{ds}^* \quad (45)$$

$$i_{ds}^* = i_{ds} (p^2 2T_{rd}^2 + p2T_{rd} + 1). \quad (46)$$

Here, $K_{\lambda r}$ represents the PI controller for the rotor flux outer-loop control and $\delta_{\lambda r}$ stands for the output of $K_{\lambda r}$. Substituting Equation 46 into Equation 45 yields Equation 47. However, from Equation 8, i_{ds}^* can be represented as Equation 48, which can be substituted in Equation 47 to yield Equation 49.

$$\delta_{\lambda r} = L_m r_r i_{ds}^* (p^2 2T_{rd}^2 + p2T_{rd} + 1). \quad (47)$$

$$i_{ds}^* = \frac{1}{L_m} (\lambda_{dr} - L_r i_{dr}). \quad (48)$$

$$K_{\lambda r} (\lambda_{dr}^* - \lambda_{dr}) = r_r (\lambda_{dr} - L_r i_{dr}) (p^2 2T_{rd}^2 + p2T_{rd} + 1). \quad (49)$$

Hence, the open-loop transfer function of the flux linkage controller given that all other disturbances are equated to zero gives Equation 50.

$$H_{o\lambda r} = \frac{\lambda_r}{K_{\lambda r} (\lambda_r^* - \lambda_r)} = \frac{\lambda_r}{K_{\lambda r} e_{\lambda r}} = k_r \frac{1}{(p^2 2T_{rd}^2 + p2T_{rd} + 1)}, \quad (50)$$

where $k_r = 1/r_r$. Introducing a delay gain into Equation 50 results in Equation 51. The delay gain can represent the time constant of the filter needed for estimating the stator flux linkage.

$$H_{oe\lambda r} = k_r \frac{1}{(p^2 2T_{rd}^2 + p2T_{rd} + 1)(pT_{re} + 1)}. \quad (51)$$

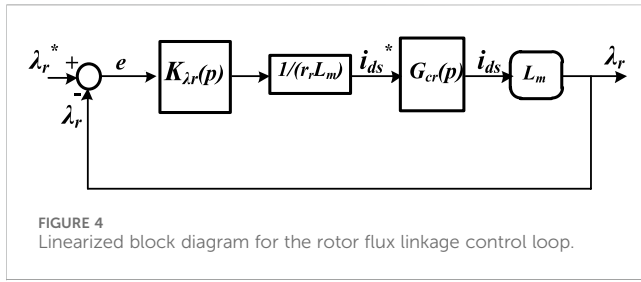


FIGURE 4 Linearized block diagram for the rotor flux linkage control loop.

$$H_{c\lambda r} = k_r \frac{K_{\lambda r}}{(p^2 2T_{rd}^2 + p 2T_{rd} + 1)(pT_{re} + 1) + k_r K_{\lambda r}} \quad (52)$$

The closed-loop transfer function is given in Equation 52. For pole-zero cancellation, let the PI controller design take the form $K_{p\lambda r}/K_{i\lambda r} = L_r/r_r$ (Lascu et al., 2007). The gains of the PI controller are expressed in Equation 53, which translates to Equation 54.

$$K_{\lambda r} = K_{p\lambda r} + \frac{K_{i\lambda r}}{p} \quad (53)$$

$$K_{\lambda r} = \frac{K_{p\lambda r}}{pT_i} (T_i p + 1) \quad (54)$$

Here, $T_i = L_r/r_r$.

Hence, appropriate substitution of Equation 54 in Equation 52, while equating that $T_i = T_{re}$, $K_{p\lambda r} = T_{re}/(2k_r T_{rd})$, and $k_r = 1/r_r$, yields Equation 55.

$$H_{c\lambda r} = \frac{1}{p^3 4T_{rd}^3 + p^2 4T_{rd}^2 + p 2T_{rd} + 1} \quad (55)$$

Notice that Equation 55 is reduced to exactly the transfer function of Equation 43 for the speed control. The stability condition, therefore, that applies for the speed loop equally suffices for the rotor flux loop control based on gains selected for both loops. A linear model of the closed-loop flux regulation is shown in Figure 4. Figure 5 shows the pole's loci for 3-time delays, $T_{rd} = 2/f_s$, $3/f_s$, and $7/f_s$ ($f_s = 5000$ Hz, switching frequency of the converters), for the optimal damping criteria in Equations 43, 55. The system is seen to be stable at a natural frequency, ω_n , which decreases as T_{rd} increases. Consequently, with more increase of T_{rd} , the closer the poles are toward marginal stability. The practical implication as such is that with a significant increase in T_{rd} , the system is tossed into instability.

6 Mechanical torque and rotor speed observer

The optimization procedure in Section 4 and the dynamic control scheme in Section 5 indicate that measuring or estimating the mechanical torque is quite vital for the efficiency optimization scheme of this article. State estimation (Awelewa et al., 2023; Omiloli et al., 2023) plays a significant role in this respect, as placing mechanical torque transducers on the drive will lead to an additional cost. Consequently, a Luenberger load torque observer is developed in this section for the energy saving scheme. The Luenberger observer block is included in the overall control scheme of the motor drive shown in Figure 6.

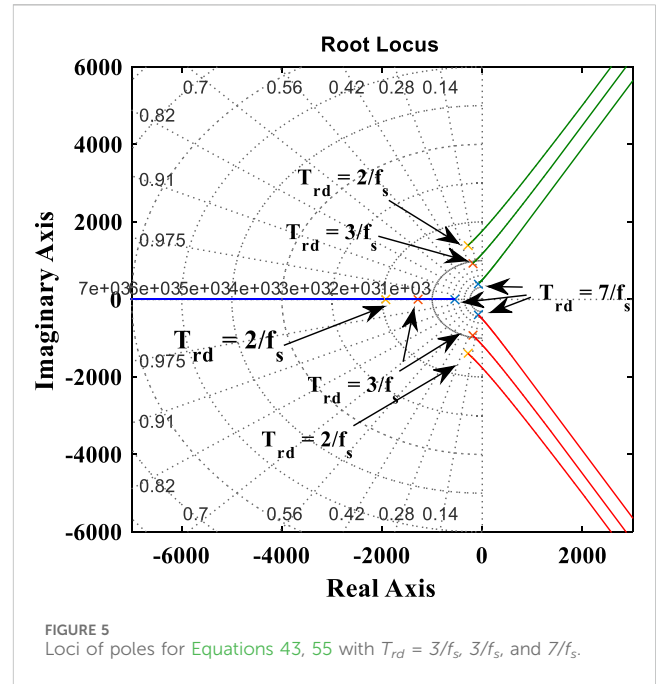


FIGURE 5 Loci of poles for Equations 43, 55 with $T_{rd} = 3/f_s$, $3/f_s$, and $7/f_s$.

6.1 State-space model

The mechanical dynamics of Equation 56 can be represented in the state-space format given in Equations 57, 58, where $x = [x_1 \ x_2]^T = [\omega_r \ T_m]^T$, $y = \omega_r$, $u = i'_{qs}$, and $C = [1 \ 0]$.

$$\begin{bmatrix} \dot{\omega}_r \\ \dot{T}_m \end{bmatrix} = \begin{bmatrix} 0 & -\frac{P}{2J} \\ 0 & 0 \end{bmatrix} \begin{bmatrix} \omega_r \\ T_m \end{bmatrix} + \begin{bmatrix} \frac{3P^2 L_m \lambda_r}{8J L_r} & 0 \\ 0 & 0 \end{bmatrix} \begin{bmatrix} i'_{qs} \\ 0 \end{bmatrix} \quad (56)$$

$$\dot{x} = Ax + Bu \quad (57)$$

$$\text{Here, } y = \omega_r, \quad u = i'_{qs}, \quad A = \begin{bmatrix} 0 & -\frac{P}{2J} \\ 0 & 0 \end{bmatrix}, \quad B = \begin{bmatrix} \frac{3P^2 L_m \lambda_r}{8J L_r} & 0 \\ 0 & 0 \end{bmatrix}, \quad \text{and } C = [1 \ 0]. \quad (58)$$

6.2 Observer model

The state-space model of sub-Section 6.1 is used to develop an observer for the mechanical load torque and consequently for the rotor speed as well. Consequently, a corresponding Luenberger observer model for Equation 56 is given in Equation 59, represented by the state-space of Equations 60, 61. Therefore, the observer herein is modified from Zorgani et al. (2016) for the rotor field-oriented control. The diagrammatic representation for the load torque and rotor speed Luenberger observer is shown in Figure 7.

$$\begin{bmatrix} \dot{\hat{\omega}}_r \\ \dot{\hat{T}}_m \end{bmatrix} = \begin{bmatrix} 0 & -\frac{P}{2J} \\ 0 & 0 \end{bmatrix} \begin{bmatrix} \hat{\omega}_r \\ \hat{T}_m \end{bmatrix} + \begin{bmatrix} \frac{3P^2 L_m \lambda_r}{8J L_r} & 0 \\ 0 & 0 \end{bmatrix} \begin{bmatrix} i'_{qs} \\ 0 \end{bmatrix} + \begin{bmatrix} L_1 \\ L_2 \end{bmatrix} (\omega_r - \hat{\omega}_r) \quad (59)$$

$$\dot{\hat{x}} = A\hat{x} + Bu + L(x - \hat{x}) \quad (60)$$

$$\hat{y} = C\hat{x} \quad (61)$$

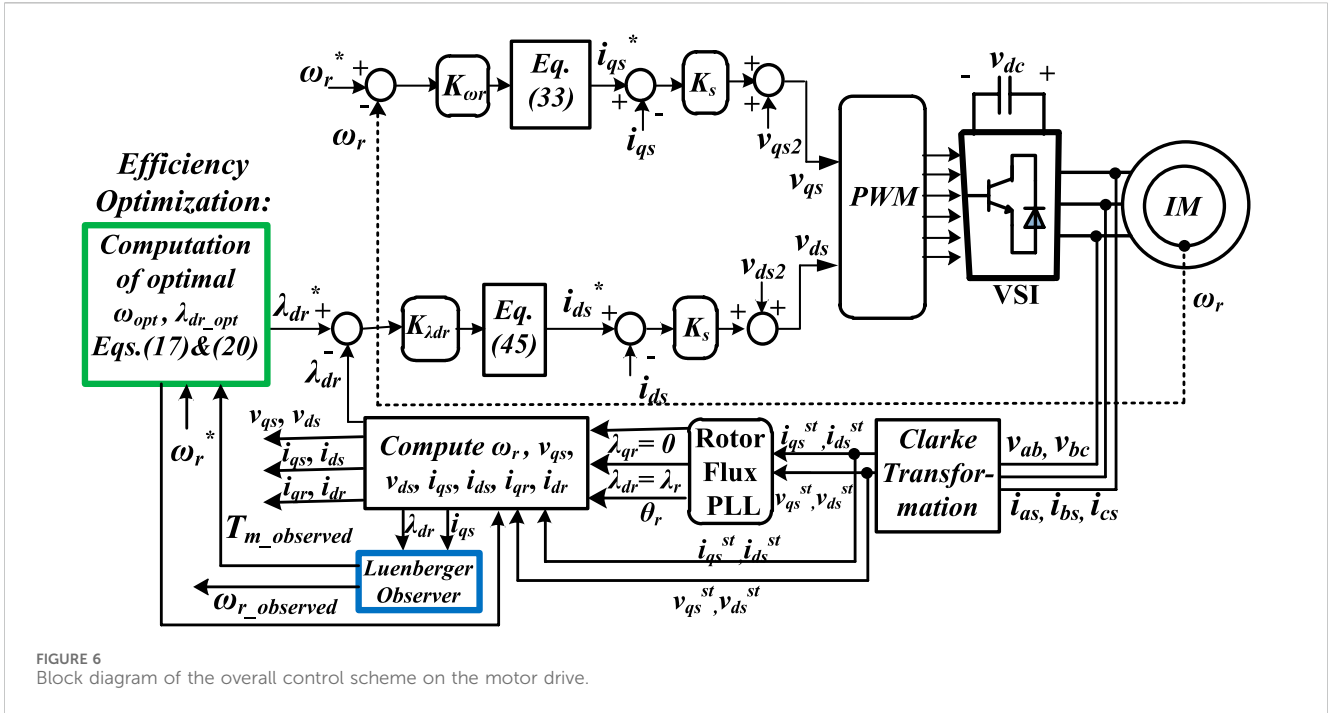


FIGURE 6 Block diagram of the overall control scheme on the motor drive.

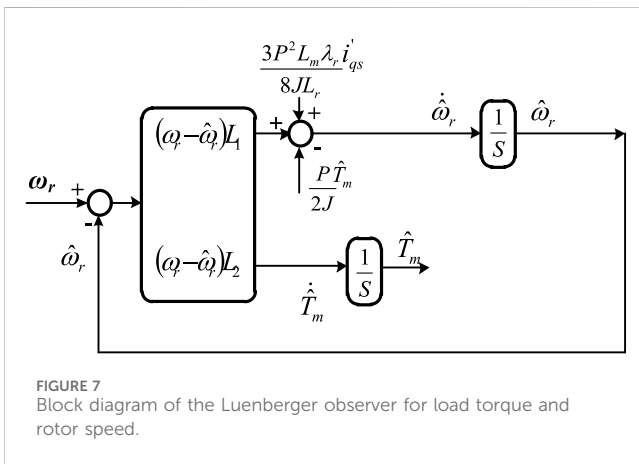


FIGURE 7 Block diagram of the Luenberger observer for load torque and rotor speed.

The error (e) between the actual state-space and state-observer models is given in Equation 62, where $\tilde{x} = e = x - \hat{x}$. In the expanded form, Equation 62 translates to Equation 63.

$$\dot{\tilde{x}} = (A - L)\tilde{x}. \tag{62}$$

$$\begin{bmatrix} \dot{\tilde{\omega}}_r \\ \dot{\tilde{T}}_m \end{bmatrix} = \begin{bmatrix} -L_1 & -\frac{P}{2J} \\ -L_2 & 0 \end{bmatrix} \begin{bmatrix} \tilde{\omega}_r \\ \tilde{T}_m \end{bmatrix}. \tag{63}$$

$$|\lambda I - (A - L)_{2 \times 2}| = 0. \tag{64}$$

The matrix $(A-L)$ in Equation 62 and consequently Equation 63 gives the characteristic equation in Equation 64, which predicts the regions of stability (Awelewa et al., 2016) and instability (if any). Solving Equation 64 gives the loci of eigenvalues at a given operating condition. Specifically, Equation 64 is further evaluated as Equation 65 that bifurcates into two distinct roots given in Equation 66. As such, stability can only be guaranteed when the eigenvalues λ_1 and λ_2 given in Equation 66 are negative definite along the real axis of the

eigenvalue locus. When L_1 is selected as positive values, L_2 must be selected as negative to maintain the negative definite eigenvalues in Equation 66. The stability limit of the observer, therefore, occurs at $L_2 = 0$, which locates λ_2 at the marginal stability of 0, while λ_1 is placed at a locus of $-L_1$. Making $L_2 > 0$ yields λ_2 to be positive definite and thereby throws the system into instability.

$$\lambda^2 + L_1 \lambda - \frac{L_2 P}{2J} = 0. \tag{65}$$

$$\lambda_{1,2} = \frac{-L_1}{2} \pm \frac{\sqrt{L_1^2 + \frac{4L_2 P}{2J}}}{2}. \tag{66}$$

Figures 8A, B were obtained from Equation 64 and give the loci of the eigenvalues that indicate stable dynamics of the observer when L_1 is fixed at 50 and L_2 is varied from -0.1 to -40 . Notice that at $L_1^2 = -4L_2 P / (2J)$, λ_1 and λ_2 become co-located on the real axis, and it implies that $L_2 = -2JL_1^2 / (4P) = -27.8125$ from the parameters given in Appendix A. Therefore, at $L_2 = -27.8125$ in Figures 8A, B, the loci of λ_1 and λ_2 can no longer extend further than $-L_1/2 = -25$ into the negative real axis but rather diverge into the imaginary axis as L_2 becomes more negative.

6.3 Primary rotor speed estimation for the observer model

Referring to (59), $\hat{\omega}_r$ is the estimated rotor speed by the Luenberger observer, while ω_r could be the rotor speed measured by a speed encoder when only the mechanical torque is of interest for estimation. However, when both the mechanical torque and the rotor speed are desired to be observed, then ω_r in Equation 59 becomes an estimate from other means, as implied in Zorgani et al. (2016) when mechanical observers are not required. In consideration of the latter, a lower-order observer can be

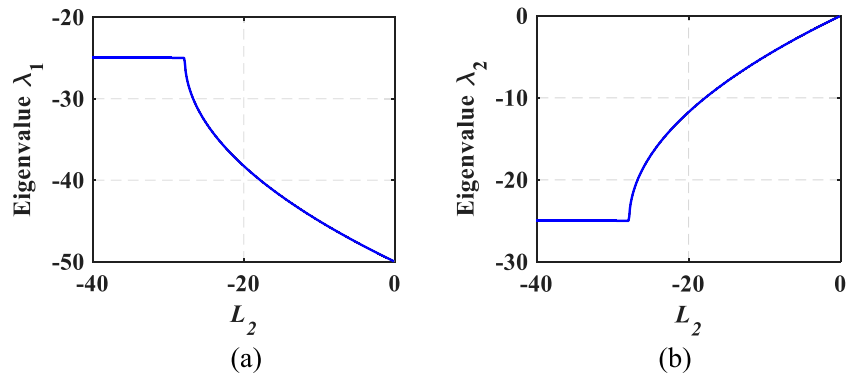


FIGURE 8 Eigenvalues from $|\lambda I - (A - L)_{2 \times 2}| = 0$: (A) real of eigenvalue loci of λ_1 against L_2 . (B) Real of eigenvalue loci of λ_2 against L_2 .

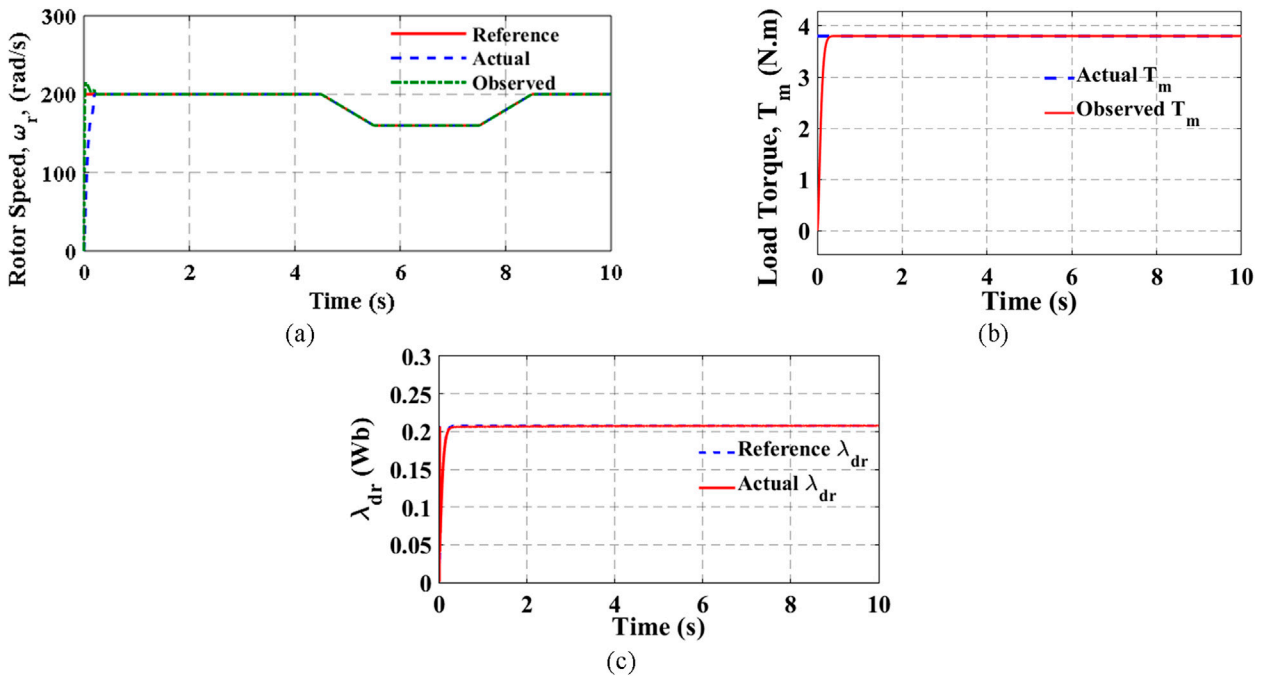


FIGURE 9 (A) Rotor speed: actual and estimated. (B) Load torque: actual and estimated. (C) Rotor flux linkage: reference and actual.

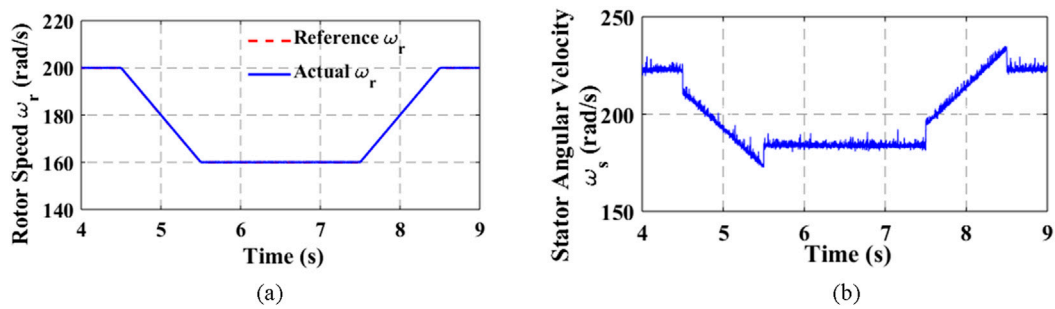
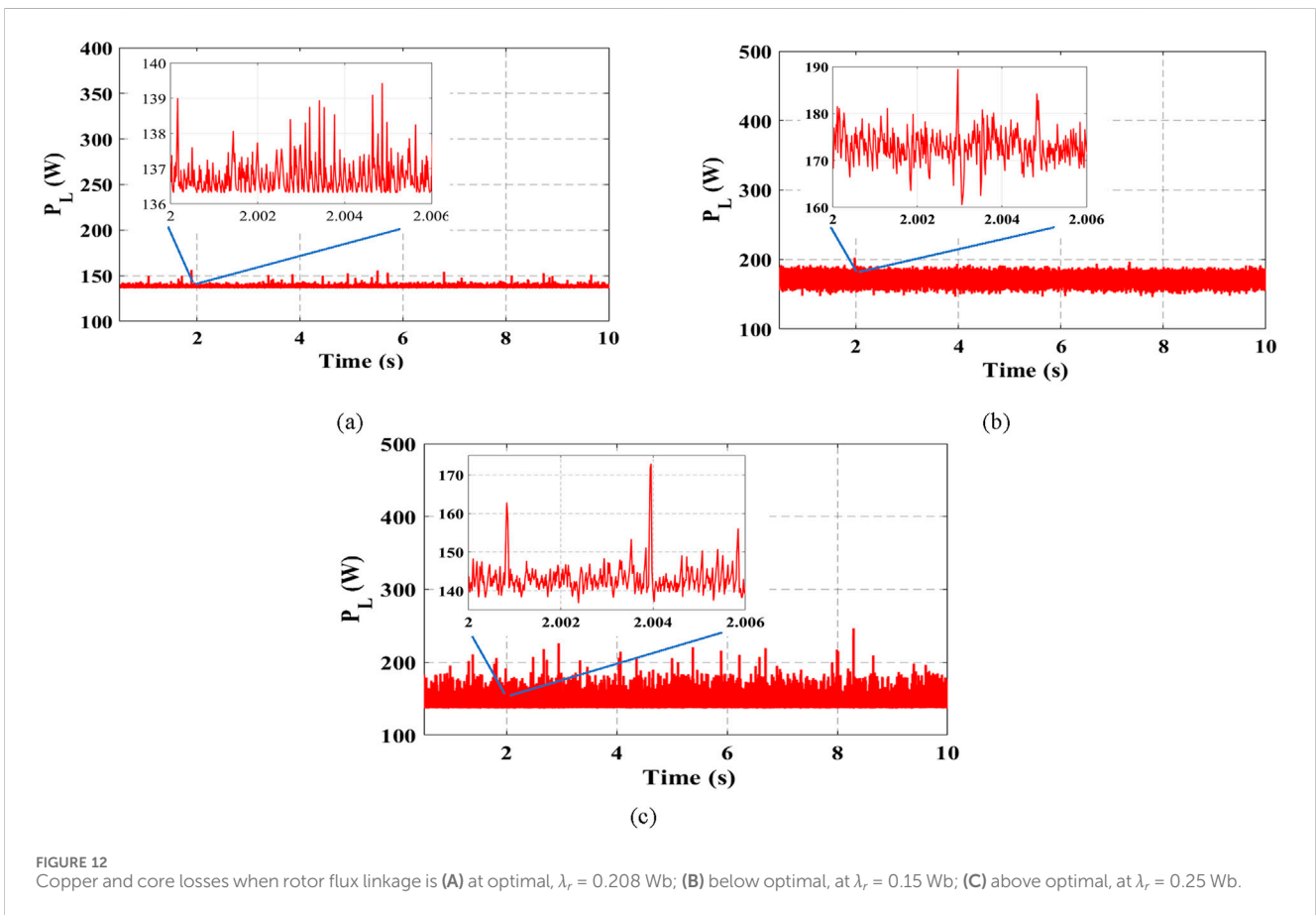
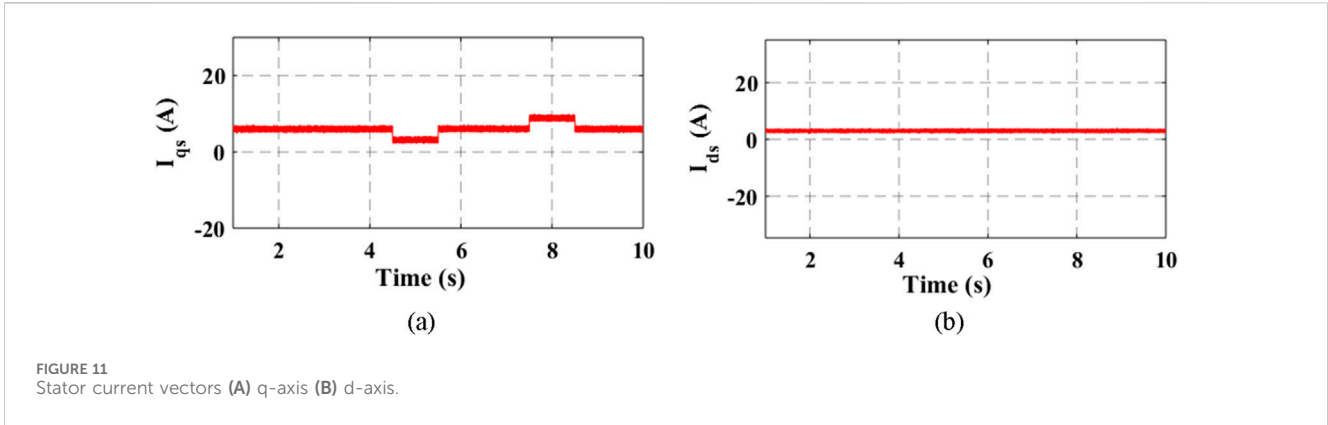


FIGURE 10 (A) Steady-state rotor speed: reference and actual. (B) Optimal stator angular velocity.



developed from Equation 3, as given in Equation 67, for ω_r , which can be substituted in Equation 59. The stator angular velocity, ω , may be determined by developing a flux phase-locked loop (flux PLL) that will give the slip angular velocity and corresponding slip angular displacement that will ensure that $\lambda_{qr} = 0$. Consequently, the reference rotor speed can be added to the slip angular velocity to extract out the precise ω and θ that achieves such an orientation. Alternatively, using Equation 3 to dynamically regulate the q-axis of the rotor flux linkage to 0 will give ω , such that ω_r in Equation 59 is taken as the rotor reference speed. The two methods have been explored during the project of

this paper. However, the details of the two methods are not within the scope of this article.

$$\omega_{r_est} = \omega + \frac{r_r i_{qr}}{\lambda_{dr}} \tag{67}$$

7 Results and discussion

The dynamic sensorless efficiency optimization-based vector control with the torque observer developed in this paper for the

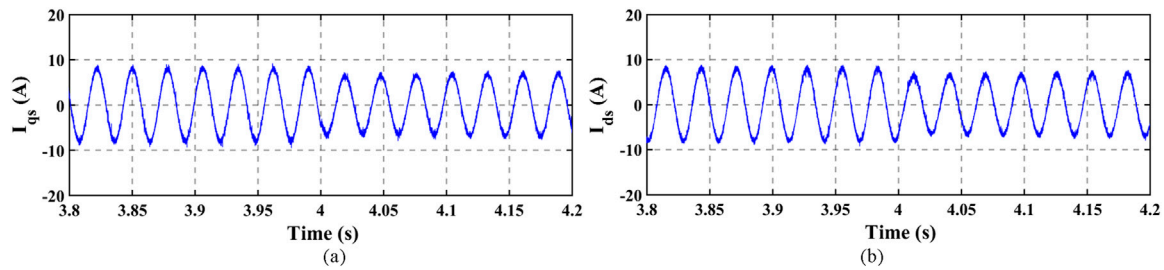


FIGURE 13 Stator stationary q-d reference frame currents in vector control: (A) I_{qs} and (B) I_{ds} .

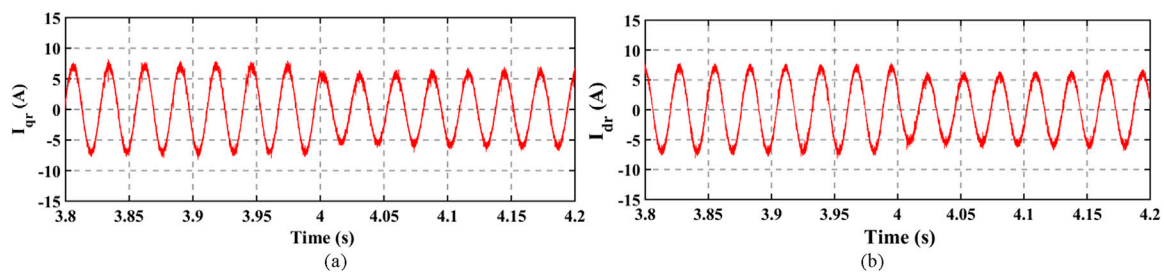


FIGURE 14 Rotor stationary q-d reference frame currents in vector control: (A) I_{qr} and (B) I_{dr} .

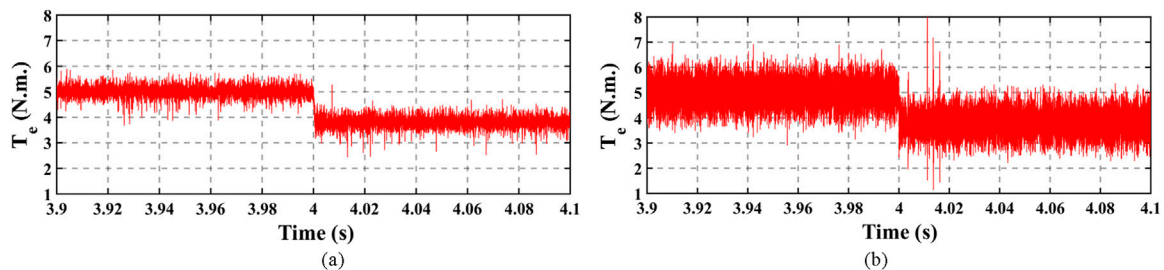


FIGURE 15 Electromagnetic torque: (A) from vector control and (B) from model predictive control.

induction motor drive was simulated in the MATLAB/Simulink environment. The simulation was carried out in two different operations. The results obtained for both operations are presented herein.

In the first operating condition, the reference rotor speed was set at 200 rad/s, while the load torque was set at 3.8 N.m. Under this condition, the rotor flux was set to pick its reference from the optimal value in Equation 20, which emanated from the optimization procedure. Then, at steady state between 4.5 s and 5.5 s, the rotor speed was ramped down from 200 rad/s to approximately 160 rad/s. After the duration of 2 s, the rotor speed was ramped back up to 200 rad/s between 7.5 s and 8.5 s. In Figures 9A–C, the rotor speed, load torque, and rotor flux linkage from the start-up to steady-state are shown. The Luenberger load

torque observer gives the estimated rotor speed and estimated load torque in Figures 9A, B, respectively. In Figure 9A, the actual and observed ω_r are seen to follow the reference command closely despite the ramp from the reference. Similarly in Figure 9B, the estimated load torque can be seen to follow the actual value closely. In Figure 10A the ramped rotor speed is shown at steady state only.

The corresponding stator angular velocity (ω_s) to Figure 10A that will guarantee optimal operation is shown in Figure 10B. The ω_s at the stator in Figure 10B is at a trajectory that gives a constant slip operation at the minimal copper and core loss regime. The q-d stator currents controlled in the inner-loop regulation are seen in Figures 11A, B respectively. Notice that in Figure 11A, the q-axis stator current maintained a steady value before and after the ramping down and ramping up. As such, a constant

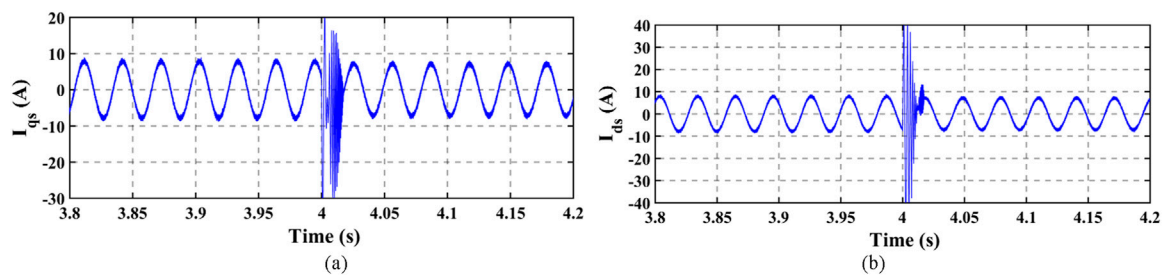


FIGURE 16 Stator stationary q-d reference frame currents in model predictive control: (A) I_{qs} and (B) I_{ds} .

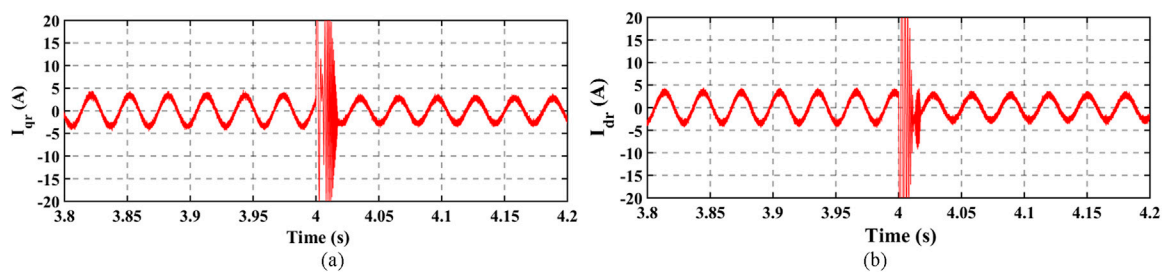


FIGURE 17 Rotor stationary q-d reference frame currents in model predictive control: (A) I_{qr} and (B) I_{dr} .

electromagnetic torque build-up is achieved for picking up the load torque that has been maintained constant. Therefore, it can be inferred in the optimization procedure developed that the load torque and not the rotor speed trajectory influences the choice of optimal rotor flux linkage. It can be deduced in the denominator of Equation 20 that if constant slip is maintained, as shown in Figures 11A, B, the load torque principally determines the choice of optimal rotor flux.

In the second operation, the rotor speed and the load torque were maintained constant at 200 rad/s and 3.8 N.m, respectively, for the entire simulation. Then, the simulation was carried out with the rotor flux linkage set at the optimal value given in Equation 2 and later changed to values below and above the optimal. The reason for such is to investigate the influence of the rotor flux on the loss regime. Figures 12A–C give the loss regime for the three rotor flux values. In Figures 12A–C, therefore, the copper and core losses are seen to be less distorted in Figure 12A where the rotor flux linkage was set at optimal. As such, setting the rotor flux linkage to an optimal value conserves energy consumption by the induction motor.

Furthermore, the efficacy of the developed efficiency-optimized vector control scheme was tested by comparing its results to those obtained from an equivalent induction machine drive on a model predictive control (MPC) scheme with the same set values of the optimal stator angular velocity and optimal rotor flux linkage. The MPC was developed in the stationary reference frame, but the details of developing the MPC are not within the scope of this article, but may be derived from previous studies (Agoro et al., 2018; Zhou et al., 2018; Mao et al., 2021; Rodas et al., 2021; Ouari et al., 2022; Wen

et al., 2022; Yang et al., 2022; Liu et al., 2019; Zhang et al., 2019). Consequently, the stator currents and rotor currents in the developed energy-saving vector control scheme were transformed from the synchronous reference frame into the stationary reference frame for comparative analysis with those obtained from the MPC.

In obtaining the comparative results, the rotor speed was maintained constant at 200 rad/s, while the load torque was stepped from 5 N.m. to 3.8 N.m at 4 s. The stator currents, rotor currents, and electromagnetic torque obtained from the developed energy saving vector control scheme are shown in Figures 13, 14, 15A respectively. However, Figures 15B, 16, 17 show the electromagnetic torque, stator currents, and rotor currents. In comparing Figures 13–17, smooth transitions were noticed when the step change in the load torque was introduced from at 4 s. The vector control effectively dampened the overshoots, which were evident in the MPC. Moreover, the harmonic contents from the vector control scheme were not as significant as those from the MPC scheme. As such, the ripples in the electromagnetic torque from the vector control scheme shown in Figure 15A are much lower than those in Figure 15B from the MPC. The reason for such could be because the switching actions in the switching semiconductor devices (e.g., MOSFET and IGBT) of the inverter–motor drive on the vector control are symmetrical, but the switching actions by the MPC are asymmetrical, which could result in the more significant ripples in the machine’s electromagnetic torque from the MPC. However, it is seen from Figures 14, 17 that the rotor currents from MPC are lower than those from the vector control, which may be due to the cost function minimization inherent in the MPC that selects the optimal switching states that gives the minimal cost function. Consequently, more reduction in the electrical loss

profile can still be experienced in the MPC, but the symmetrical switching in vector control gives the edge of healthier electromagnetic torque development.

8 Conclusion

A vector control scheme for an induction motor drive has been presented in this paper. The scheme guarantees an optimal operating regime for the induction motor based on an appropriate choice of optimal reference for the rotor flux linkage, as any choice of the rotor flux linkage, which is above or below the optimal values, will lead to more copper and core losses and more harmonic distortions in the machine variables. Since the machine load torque aids the determination of this optimal reference, and the rotor speed does not play any active role in the choice of such optimal rotor flux linkage if the slip is maintained constant, a Luenberger observer is developed to estimate the load torque. In the comparative analysis with the MPC, though the energy-saving vector control yielded more rotor currents that may imply a slight increase in the loss regime, the vector control gave lower ripples and consequently healthier electromagnetic torque in the induction machine. Furthermore, the vector control scheme rode through the step change in load torque smoothly, which the MPC was unable to attain.

Data availability statement

The original contributions presented in the study are included in the article/Supplementary Material; further inquiries can be directed to the corresponding author.

Author contributions

AB: conceptualization, methodology, writing–original draft, and writing–review and editing. AO: investigation, methodology,

software, and writing–review and editing. AA: funding acquisition, investigation, software, and writing–review and editing. FO: methodology, supervision, and writing–review and editing. TS: funding acquisition, investigation, software, and writing–review and editing. IS: funding acquisition, methodology, and writing–review and editing.

Funding

The author(s) declare that no financial support was received for the research, authorship, and/or publication of this article.

Acknowledgments

The authors acknowledge and appreciate technical support given to this project by the University of Lagos. The authors also deeply recognize the assistance given by Covenant University in all aspects of this research, especially the payment of the publication charges.

Conflict of interest

The authors declare that the research was conducted in the absence of any commercial or financial relationships that could be construed as a potential conflict of interest.

Publisher's note

All claims expressed in this article are solely those of the authors and do not necessarily represent those of their affiliated organizations, or those of the publisher, the editors, and the reviewers. Any product that may be evaluated in this article, or claim that may be made by its manufacturer, is not guaranteed or endorsed by the publisher.

References

- Abrahamsen, F., Blaabjerg, F., Pedersen, J. K., and Thøgersen, P. B. (2001). Efficiency-optimized control of medium-size induction motor drives. *IEEE Trans. Ind. Appl.* 37 (6), 1761–1767. doi:10.1109/28.968189
- Abrahamsen, F., Pedersen, J. K., and Blaabjerg, F. (1996). State-of-art of optimal efficiency control of low cost induction motor drives. *Proc. PEMC 2*, 163–170.
- Agoro, S., Balogun, A., Ojo, O., and Okafor, F. (2018). “Direct model-based predictive control of a three-phase grid connected VSI for photovoltaic power evacuation,” in proceedings of 9th IEEE International Symposium on Power Electronics for Distributed Generation Systems (PEDG), 1–6.
- Akin, B., Orguner, U., and Ersak, A. (2004). A comparative study on Kalman filtering techniques for state estimation of industrial AC drive systems. *Proc. IEEE Int. Conf. Mechatronics, 2004. ICM '04.* 12, 439–445. doi:10.1109/ICMECH.2004.1364479
- Ali, M. T., Zhou, D., Song, Y., Ghandhari, M., Harnefors, L., and Blaabjerg, F. (2020). Analysis and mitigation of SSCI in DFIG systems with experimental validation. *IEEE Trans. Energy Convers.* 35 (2), 714–723. doi:10.1109/tec.2019.2953976
- Almeida, D. D. S., Filho, W. C. P. D. A., and Sausa, G. C. D. (2007). Adaptive fuzzy controller for efficiency optimization of induction motors. *IEEE transaction Industrial Mot.* 54 (4), 2157–2164.
- Awelewa, A., Omiloli, K., Samuel, I., Ojajube, A., and Popoola, O. (2023). Robust hybrid estimator for the state of charge of a lithium-ion battery. *Front. Energy Res.* 10, 1–11. doi:10.3389/fenrg.2022.1069364
- Awelewa, A. A., Awosope, C. O. A., Abdulkareem, A., and Samuel, I. (2016). Nonlinear control laws for electric power system stabilization. *J. Eng. Appl. Sci.* 11 (7), 1525–1531.
- Balogun, A., Ojo, O., and Okafor, F. (2021). Efficiency optimization control of doubly-fed induction generator transitioning into shorted-stator mode for extended low wind speed application. *IEEE Trans. Industrial Electron.* 68 (12), 12218–12228. doi:10.1109/tie.2020.3037990
- Blanusa, B. (2010). *New trends in efficiency optimization of induction motor drives.* bosnia and herzegovina: university of banja luka.
- Bose, B. K., Patel, N. R., and Rajashekara, K. (1997). A neuro-fuzzy-based online efficiency optimization control of a stator flux-oriented direct vectorcontrolled induction motor drive. *IEEE Trans. Ind. Electron.* 44 (2), 270–273. doi:10.1109/41.564168
- Chakraborty, C., and Hori, Y. (2003). Fast efficiency optimization techniques for the indirect vector-controlled induction motor drives. *IEEE Trans. Ind. Appl.* 39 (4), 1070–1076. doi:10.1109/tia.2003.814550
- Chakraborty, C., Ta, M. C., and Hori, Y. (2003). Speed sensorless, efficiency optimized control of induction motor drives suitable for EV applications. *Proc. IEEE IECON* 1, 913–918. doi:10.1109/iecon.2003.1280105
- Choudhary, P. K., Dubeyand, S. P., and Gupta, V. K. (2015). Efficiency optimization of induction motor drive at steady-state condition. *2015 Int. Conf. Control, Instrum.*

- Commun. Comput. Technol. (ICCICT) 54, 470–475. doi:10.1109/ICCICT.2015.7475325
- Dong, G., and Ojo, O. (2006). Efficiency optimizing control of induction motor using natural variables. *IEEE Trans. Industrial Electron.* 53 (6), 1791–1798. doi:10.1109/tie.2006.885117
- Ghozzindall, S., Jelassi, K., and Roboam, X. (2004). Energy optimization of induction motor drives. *IEEE Int. Conf. Industrial Technol. (ICIT)* 2, 602–610. doi:10.1109/icit.2004.1490143
- Gong, C., Hu, Y., Ni, K., Liu, J. J., and Gao, J. (2019). SM load torque observer-based FCS-MPDS with single prediction horizon for high dynamics of surface-mounted PMSM. *IEEE Trans. Power Electron.* 35 (1), 20–24. doi:10.1109/tpe.2019.2929714
- Holmes, D. G., Lipo, T. A., Kong, W. Y., and McGrath, B. P. (2009). Optimized design of stationary frame three phase AC current regulators. *IEEE Trans. Power Electron.* 24 (11), 2417–2426. doi:10.1109/tpe.2009.2029548
- Kastha, D., and Bose, B. K. (1995). On-line search based pulsating torque compensation of a fault mode single-phase variable frequency induction motor drive. *IEEE Trans. Industry Appl.* 31 (4), 802–811. doi:10.1109/28.395290
- Kazmierkowski, M. P., Krishnan, R., and Blaabjerg, F. (2002). *Control in power electronics: selected problems*. London: Acad. Press, 190–207.
- Kirischen, D. S., Novoty, D. W., Lipo, T. A., and March (1987). Optimal efficiency control of an induction motor drive. *IEEE Trans. Energy Convers.* EC-2 (1), 70–76. doi:10.1109/tec.1987.4765806
- Kirschen, D. S., Novoty, D. W., and Lipo, T. A. (1985). On line efficiency optimization of a variable frequency induction-motor drive. *IEEE Trans. Ind. Appl.* IA-21 (3), 610–616. doi:10.1109/tia.1985.349717
- Kirschen, D. S., Novoty, D. W., and Suwanisoot, W. (1984). Minimizing induction motor losses by excitation control in variable frequency drives. *IEEE Trans. Ind. Appl.* IA-20 (5), 1244–1250. doi:10.1109/tia.1984.4504590
- Kumar, N., Chelliah, T. R., and Srivastava, S. S. (2014). Adaptive control schemes for improving dynamic performance of efficiency-optimized induction motor drives. *ISA Trans.* 57, 301–310.
- Lascu, C., Asiminoaei, L., Boldea, I., and Blaabjerg, F. (2007). High performance current controller for selective harmonic compensation in active power filters. *IEEE Trans. Power Electron.* 22 (5), 1826–1835. doi:10.1109/tpe.2007.904060
- Lascu, C., and Trzynadlowski, A. M. (2004). Combining the principles of sliding mode, direct torque control, and space-vector modulation in a high-performance sensorless AC drive. *IEEE Trans. Industry Appl.* 40 (1), 170–177. doi:10.1109/TIA.2003.821667
- Liu, M., Chan, K. W., Hu, J., Xu, W., and Rodriguez, J. (2019). Model predictive direct speed control with torque oscillation reduction for PMSM drives. *IEEE Trans. Industrial Inf.* 15 (9), 4944–4956. doi:10.1109/tii.2019.2898004
- Mao, J., Li, H., Yang, L., Zhang, H., Liu, L., Wang, X., et al. (2021). Non-cascaded model-free predictive speed control of SMPMSM drive system. *IEEE Trans. Energy Convers.* 37 (1), 153–162. doi:10.1109/tec.2021.3090427
- Moreno-Eguilaz, J. M., and Peracaula, J. (1999). Efficiency optimization for induction motor drives: past, present and future. *Proc. Electrimes*, 1187–1191.
- Olajube, A., and Anubi, O. M. (2023). “Model-based loss minimization control of a squirrel cage induction motor drive with shorted rotor under indirect field orientation,” in 2023 IEEE Conference on Control Technology and Applications (CCTA), Bridgetown, Barbados (IEEE), 759–765.
- Omiloli, K., Awelewa, A., Samuel, I., Obiazi, O., and Katende, J. (2023). State of charge estimation based on a modified extended Kalman filter. *Int. J. Electr. Comput. Eng.* 13 (5), 5054–5065. doi:10.11591/ijec.v13i5.pp5054-5065
- Ouari, K., Belkhir, Y., Djouadi, H., Kasri, A., Bajaj, M., Alsharif, M., et al. (2022). Improved nonlinear generalized model predictive control for robustness and power enhancement of a DFIG-based wind energy converter. *Front. Energy Res.* 10, 996206. doi:10.3389/fenrg.2022.996206
- Qu, Z., Ratna, M., Hinkkanen, M., and Luomi, I. (2012). Loss-minimizing flux level control of induction motor drives. *IEEE Trans. Ind. Appl.* 48, 952–961. doi:10.1109/tia.2012.2190818
- Rabelo, B. C., Hofmann, W., da Silva, J. L., Gaiba de Oliveira, R., and Rocha Silva, S. (2009). Reactive power control design in doubly fed induction generators for wind turbines. *IEEE Trans. Industrial Electron.* 56 (10), 4154–4162. doi:10.1109/tie.2009.2028355
- Rehman, H., and Xu, L. (2011). Alternative energy vehicles drive system: control, flux and torque estimation, and efficiency optimization. *IEEE Trans. Veh. Technol.* 60 (8), 3625–3634. doi:10.1109/TVT.2011.2163537
- Rodas, J., Gonzalez-Prieto, I., Kali, Y., Saad, M., and Doval-Gandoy, J. (2021). Recent advances in model predictive and sliding mode current control techniques of multiphase induction machines. *Front. Energy Res.* 9, 729034. doi:10.3389/fenrg.2021.729034
- Sajedi, S., Khalifeh, F., Khalifeh, Z., and karimi, T. (2011). Application of Particle swarm Optimization and Genetic Algorithm methods for vector control of induction motor. *Aust. J. Basic Appl. Sci.* 5 (12), 1697–1706.
- Sousa, G. C. D., Bose, B. K., and Cleland, J. G. (1995). Fuzzy logic based on-line efficiency optimization control of an indirect vector-controlled induction motor drive. *IEEE Trans. Ind. Electron.* 42 (2), 192–198. doi:10.1109/41.370386
- Sousa, G. C. D., Bose, B. K., Cleland, J. G., Spiegel, R. J., and Chappell, P. J. (1992). Loss modeling of converter induction machine system for variable speed drive. *Proc. IEEE IECON* 115, 114–120. doi:10.1109/iecon.1992.254595
- Stumper, J. F., Dotlinger, A., and Kennel, R. (2013). Loss minimization of induction machines in dynamic operation. *IEEE Trans. energy Convers.* 28 (3), 726–735. doi:10.1109/tec.2013.2262048
- Sul, S. K., and Park, M. H. (1988). A novel technique for optimal efficiency control of a current source inverter fed induction motor. *IEEE Trans. Power Electron.* 3 (2), 192–199. doi:10.1109/63.4349
- Ta-Cao, M., and Hori, Y. (2000). “Convergence improvement of efficiency optimization control of induction motor drives,” in Proc. IEEE IASAnnu.Meeting, Rome, Italy.
- Uddin, M. N., and Nam, S. W. (2008). Development of a nonlinear and model-based online loss minimization control of an IM drive. *IEEE Trans. Energy Convers.* 23 (4), 1015–1024. doi:10.1109/TEC.2008.2001442
- Uddin, M. N., Rahman, M. M., Patel, B., and Venkatesh, B. (2019). Performance of a loss model based nonlinear controller for IPMSM drive incorporating parameter uncertainties. *IEEE Trans. Power Electron.* 34 (6), 5684–5696. doi:10.1109/TPEL.2018.2871033
- Vukosavic, S. N., and Levi, E. (2003). Robust DSP-based efficiency optimization of a variable speed induction motor drive. *IEEE Trans. Ind. Electron.* 50 (3), 560–570. doi:10.1109/tie.2003.812468
- Wen, X., Wu, T., Jiang, H., Peng, J., and Wang, H. (2022). MPC-based control strategy of PV grid connected inverter for damping power oscillations. *Front. Energy Res.* 10, 968910. doi:10.3389/fenrg.2022.968910
- Yang, L., Li, H., Huang, J., Zhang, Z., and Zhao, H. (2022). Model predictive direct speed control with novel cost function for SMPMSM drives. *IEEE Trans. Power Electron.* 37 (8), 9586–9595. doi:10.1109/tpe.2022.3155465
- Zhang, X., Cheng, Y., Zhao, Z., and He, Y. (2019). Robust model predictive direct speed control for SPMSM drives based on full parameter disturbances and load observer. *IEEE Trans. Power Electron.* 35 (8), 8361–8373. doi:10.1109/tpe.2019.2962857
- Zhou, Y., Li, H., and Zhang, H. (2018). Model-free deadbeat predictive current control of a surface-mounted permanent magnet synchronous motor drive system. *J. Power Electron.* 18 (1), 103–115.
- Zorgani, Y. A., Koubaa, Y., and Boussak, M. (2016). MRAS state estimator for speed sensorless ISFOC induction motor drives with Luenberger load torque estimation. *ISA Trans.* 61, 308–317. doi:10.1016/j.isatra.2015.12.015

Appendix

Machine parameters

A 3 hp, 1,710 rpm, 220-V line-line (rms), 60 Hz, 4-pole squirrel cage induction machine; stator resistance (r_s) 0.435 Ω ; rotor referred

resistance (r_r) 0.816 Ω ; stator leakage inductance (L_{ls}) 0.002 H; rotor referred leakage inductance (L_{lr}) 0.002 H; magnetizing inductance (L_m) 0.0693 H; core loss resistance (r_c) 850 Ω ; inertia (J) 0.089 kg.m²; rated torque 11.9 N.m.

Nomenclature

| | |
|---------------------------------|--|
| v_{qs} , v_{ds} | q and d stator voltages |
| i_{qs} , i_{ds} | q and d stator currents |
| i_{qs}^* , i_{ds}^* | Torque producing q and d stator currents |
| λ_{qs} , λ_{ds} | q and d stator flux linkages |
| v_{qr} , v_{dr} | q and d stator referred rotor voltages |
| i_{qr} , i_{dr} | q and d stator referred rotor currents |
| λ_{qr} , λ_{dr} | q and d stator referred rotor flux linkages |
| i_{cp} , i_{cd} | q and d core loss currents |
| ω , ω_e | Angular velocity in arbitrary and synchronous frames |
| ω_r , ω_s | Rotor speed and stator angular velocity |
| L_s , L_r | Stator and stator referred rotor self-inductances |
| r_s , r_r | Stator and stator referred rotor resistance |
| r_c | Core loss resistance |
| L_m | Magnetizing inductance (3/2 in value) |
| VSI | Voltage source inverter |
| T_e , T_m | Electromagnetic torque and mechanical torque |
| P_L | Core and copper losses |
| m_{qp} , m_{dr} | VSI's q and d modulation index for CB-PWM |
| v_{dc} | direct current (DC) link voltage |
| C_d | DC link capacitor |
| i_o | Rectifier's DC output current |
| i_d | VSI's DC input current |
| P , J | Machine's number of poles, machine's inertia |
| P | Operator, $p = d/dt$ |